Advanced Engineering Materials

ADVANCED ENGINEERING MATERIALS
www.aem-journal.com

RESEARCH ARTICLE OPEN ACCESS

Deterministic Detection of Single Ion Implantation

Mason Adshead[1] | Lok Kan Wan[1] | Maddison Coke[1] | Janet Jacobs[1] | Nicholas F. L. Collins[1] | Mark C. Rosamond[2] | Richard J. Curry[1]

[1]Department of Electrical and Electronic Engineering, Photon Science Institute, University of Manchester, Manchester, UK | [2]School of Electronic and Electrical Engineering, University of Leeds, Leeds, UK

Correspondence: Mason Adshead (mason.adshead@manchester.ac.uk)

Received: 10 November 2025 | **Revised:** 10 February 2026 | **Accepted:** 27 February 2026

Keywords: deterministic | ion implantation | qubits

ABSTRACT

Single ion implantation using focused ion beam systems enables high spatial resolution and maskless doping for rapid and scalable engineering of materials for quantum technologies, particularly for the generation of qubits and colour centres in solid-state hosts. In these applications, the confidence with which a single ion can be deterministically implanted is critical, and so the efficiency of the detection mechanism is a vital parameter to understand. Here, we present a study of the single ion detection efficiency for a variety of ion species (Si, P, Mn, Co, Ge, Sb, Au, and Bi) into various hosts (Si, SiO_2, Al_2O_3, GaAs, diamond, and SiC). The effect of varying ion mass, charge, and kinetic energy is studied, in addition to the cluster implantation of Sb, Au, and Bi. The detection efficiencies measured vary from 40% to 100%, based on the substrate and ion beam combination.We demonstrate that it is possible to achieve detection efficiencies >90% for a wide range of ion species and substrate combinations through selection of the implantation parameters. Furthermore, detection efficiencies of 100% are found for the doping of Sb clusters, which is of direct relevance for the future fabrication of quantum devices.

1 | Introduction

The realisation of robust methods for fabricating buried donor-ion solid-state qubit technologies is essential to enable their scaling into large arrays to realise fault-tolerant quantum computing. Large numbers of physical qubits (∼1 million) are required in order to employ quantum error correction protocols, and to deliver the number of logical qubits required to demonstrate quantum supremacy [1]. Achieving this capability within solid-state hosts requires the placement of dopants with high spatial precision and with low doping error rates, meaning large-area bulk doping methods such as gas-assisted deposition and doping during substrate growth are unsuitable. Lithographic methods based on scanning tunnelling microscopy have the necessary high precision placement of dopants and have been utilised in the formation of a two-qubit gate device [2]. However they present challenges in scaling in order to deliver the very large arrays required. They are also subject to the stochastic nature of dopant formation, meaning that clusters of ions can form when only a single ion is desired [3]. Ion implantation as a versatile and scalable technique for solid-state doping is well established. It has been successfully used to create physical qubits via low-dose broad beam doping using nano-scale windows in resist [4] and a movable nano-aperture [5], which provide the crucial high-resolution spatial positioning of the ions. Recent advances in focused ion beam (FIB) doping have enabled its application to demonstrate functionality aligned with the scalable delivery of quantum technologies [6]. These include localised isotopic enrichment of ^{28}Si to provide nuclear-spin-free hosts for donor ion qubits [7, 8] and the fabrication of large arrays of single-photon emitters with high spatial positioning resolution in diamond substrates [9]. Suggested qubit device architectures, such as the flip-flop architecture [10], enable relatively long distance coupling of nuclear spins (over hundreds of nm), relaxing the constraint on atomic spatial resolution to something more routinely achievable with FIB systems. FIB implantation therefore provides an attractive methodology for the scalable doping of donor

ions within solid-state materials for qubit formation. The utilisation of FIB implantation is also attractive in other technology areas where the ability to perform local modification of a material's properties can be utilised. This, for example, includes the doping and modification of epitaxial quantum dot systems [11, 12] and the direct writing of optically active emitters into non-linear hosts [13].

A critical requirement for the formation of a working array of physical qubits is to control of the number of ions doped at each location. Multiple ions at the same location can result in undesirable ion–ion interactions leading to decoherence and impacting qubit control. The ability to determine whether an ion has or has not been implanted on the single ion level is material system dependent and difficult to confirm post-implantation. For example, colour centres can be created in silicon [14] and diamond [15] by ion implantation and their emission studied. These systems, however, often have low formation and activation efficiencies [14, 16], less than unity photoluminescence quantum efficiency and collection efficiency, and so are not suitable for accurately determining the number of ions implanted.

Scanning transmission electron microscopy (STEM) can image the atomic-scale incorporation of dopant ions within a thin membrane of material [6]. However, in order to image enough ions for robust statistical analysis of deterministic implantation, the size of the areas under investigation in STEM needs to be much larger than 10s of nm, which typical field of view sizes are limited to. In experiments such as the ones conducted in this work, regions of 10s ofμm would need to be imaged with atomic resolution to determine whether an ion is located in a position where a successful ion implantation signal was recorded. Novel STEM systems are being developed in order to scan larger regions of membranes with atomic resolution which will be invaluable in verification of the detection efficiency. This will still be limited to membrane-type substrates with high mass contrast between the membrane and implanted ion, being necessary for high-quality data. Membranes are required as forming STEM-compatible samples from bulk substrates used for quantum device fabrication will be inherently destructive to the device. It is therefore essential to develop in situ methods to determine whether an ion has been implanted into a substrate during the implantation process itself.

A detailed study of the experimental factors that govern the deterministic doping of single ions is given by Murdin, et al. [17] with single-ion detection being a key requirement. The detection of single-ion implantation events into solid-state substrates, such as diamond and silicon, can be performed using ion beam-induced charge (IBIC) detection. This relies on the detection of electron–hole pairs generated within the material by the implanted ion, using an electric field to sweep the carriers to their, respectively, polarised electrodes on the substrate surface (or bottom side). Single ion detection efficiencies using this approach have been reported as 85.5% in graphene-enhanced diamond [18], and from 87.6% up to >99% in Si-based detectors [19, 20] for ion implantation energies in the range of 10s of keV. However, despite the high efficiencies achieved, the requirement to fabricate in-built IBIC detectors within the target materials adds complexity and cost that often precludes them from being integrated and scaled to produce large array devices.

An alternative approach to single ion implantation detection utilises the secondary electrons ejected from the surface of a substrate as a consequence of ion implantation with high-sensitivity secondary electron detectors (SEDs). This method of emitted secondary electron detection does not require any additional processing, e.g., electrode deposition for device fabrication, and therefore offers a simple method applicable irrespective of the target substrate. Cassidy, et al. [21] previously investigated the SED detection efficiency of Bi ion implantation into a small number of substrates, reporting detection efficiencies into silicon of up to 89 (±2)% for 50 keV Bi ions.

n this work, we report a detailed study of the influence of ion species (mass), charge state, and energy on single-ion and molecular-ion (cluster) detection efficiency into a variety of substrates. We demonstrate that through choice of implanted ion, energy, and target substrate detection efficiencies up to 100% may be achieved.

2 | Deterministic Ion Implantation

The ion implantation system used in this work (P-NAME) is described in detail elsewhere [6], but an overview of the key features pertaining to deterministic ion implantation is given here. While the spatial resolution of FIBs can be high (e.g., sub 10 nm for 50 keV Bi [6]), there are limitations to the spatial control of the final positioning within the substrate which include the straggle of the ion due to scattering during implantation, and post-implantation diffusion of the dopant in the substrate matrix, typically when annealing. The former can be controlled to some degree through choice of implantation energy (which can be simulated using Monte Carlo methods such as the Stopping and Range of Ions in Matter (SRIM) software package [22]), though the depth of implantation is also linked to the ion energy. The latter can be mitigated somewhat by controlling the annealing parameters such that dopant activation is achieved without significant diffusion of the dopant from the targeted region of implantation. Within this work, we are only concerned with ion detection efficiency; thus, used ion beam diameters of ∼100 nm for all measurements which are readily achievable for all ion species and energies studied.

Figure 1 shows a schematic of the key components of the P-NAME system. All of the utilised ion sources are metal alloys, which are resistively heated until molten and then electrostatic voltages are used to extract a steady beam of emitted ions from the tip. Such liquid metal alloy ion sources (LMAIS) are common in FIB systems with the alloy nature enabling the selection of different elements from the beam via the mass-selecting (Wien) filter, which also allows for selection of the ion charge-states. The mass resolution of the P-NAME tool enables isotopic selection of ions within the beam from each alloy, owed in part to the mass resolving apertures as previously demonstrated [6]. This is illustrated in Figure 1 by the mixed-colour line emitting from the source (mixed ion beam) separating into solid orange and pink lines (ion beams not selected) and the solid green line (the selected ion beam). The condenser lens allows for adjustment of the ion beam current, while the objective lens focuses the beam onto the substrate. The ion beam is nominally blanked inside of the column (solid green line in the schematic) by the pulser (blanking) plates. The blanking voltage on the pulser plates is removed to allow the beam to pass through the lower optics of the column and into the chamber (green sphere). With a sufficiently low ion beam current and short pulse width (time for which the beam is unblanked), the number of ions

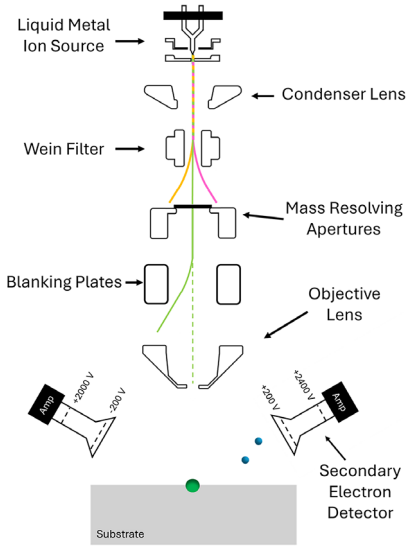

FIGURE 1 | Schematic depiction of the ion implantation system (P-NAME [6]). The mixed-isotope ion beam (orange, green and pink mixed-colour line along the optical axis) is mass-seperated by the Wien filter (deflecting unwanted beams, pink and orange solid lines) and allowing the selected ion beam (solid green line) to pass unimpeded. The ion beam is nominally blanked (solid green line, deflected) and unblanked for a determined period of time to allow a discrete number of ions (dashed green line) to implant into a substrate (green sphere) and emit secondary electrons (blue spheres). The secondary electrons are deflected into linear channeltron detectors where the signal is amplified and recorded for analysis as described within the text.

which are able to pass into the sample chamber is discrete and determined by Poissonian statistics:

$$\mathrm{P}(k) = \frac{\lambda^k e^{-\lambda}}{k!} \tag{1}$$

where $\mathrm{P}(k)$ is the probability a given pulse will contain k ions based on an average number of ions per pulse, λ:

$$\lambda = \frac{It}{q} \tag{2}$$

where I the ion beam current, t the ion pulse width, and q the ion beam species charge state (in multiples of the universal electronic charge, e).

When the ion implants into the substrate, secondary electrons are released into the vacuum of the sample chamber (blue spheres in Figure 1). The electric field between the two secondary electron detectors (SEDs) means that the electrons are attracted to the detector with positive front voltage. Details on the SED voltage configuration optimisation are provided in Supporting Information, Section S.1. The linear channeltron component of the SEDs generates an avalanche of electrons from the emitted secondary electrons, producing a signal which is then amplified by the high bandwidth electronics (proprietary, Ionoptika Ltd.). This signal is then recorded by the analysis software (via an analogue to digital converter, ADC), where the signal is analysed for a potential detection. Secondary ion emission as a consequence of ion implantation is also possible, though it is detected far less frequently. Positive ions will be deflected to the negatively polarised SED, and negative ions to the positively polarised SED (along with the electrons).

Ion beam blanking is achieved by the biasing of electrostatic plates, of 2 mm length, through which the beam passes. The bias is briefly removed for time T to create an ion pulse. The transit time of ions through the 2 mm plates, T_0, results in a necessary adjustment to the pulse width used in calculations of λ due to this switching latency ($t = T - T_0$). The implantation software records a successful implantation if the signal is: (i) above a set voltage threshold (set to 1000 mV for this work); and (ii) is within the detection window. The time at which the detection window opens is determined by velocity (energy) of the ion in question and the distance from the ion blanking plate to the target. The closing time of the window is determined by the pulse width, and extended by considering the additional time required for a secondary electron of a few eV to reach the detector. Since the mass of secondary ions are much greater than secondary electrons and are much less in number, the window timings consider the flight time of secondary electrons only.

If a signal is observed outside of this detection window, it is considered to not correlate with the pulsing of the ion beam and so these signals are considered false positives (dark counts from cosmic rays triggering an electron cascade in the linear channeltron detector, for example). A measurement of the dark count rate, performed by measuring detection with the ion beam blanked (see Experimental Methods) yields a value of 8 counts s^{-1}. This means we would expect to only record one dark count in every 595 238 pulses for the shortest pulse length used. This number of pulses is an order of magnitude more than actually used (33 773) in this study (M_i in Table 1). Likewise for the longest pulse used (2.1 µs) we expect one dark count in every 59 523 pulses compared to the 4462 pulses actually used. Therefore, the majority of detected signals within the window correspond to an ion implantation event. The ADC begins recording the amplified signal when the beam is unblanked and continues to record for a total of 40.63 µs. At this point the ADC stops recording the signal for that particular pulse and the beam deflection voltages are configured to move the beam (while blanked) to the next coordinate in the experiment. The time between the pulses is to ensure that any slow moving ions within the chamber (e.g., low energy secondary ions) do not trigger an SED response which could be mistaken for a successful implantation signal in the next pulse in the sequence.

The detection efficiency, η, characterises the confidence with which an ion or ions within a pulse result in a secondary electron signal indicating successful implantation into the target substrate. This value correlates with the secondary electron emission probability (which is, itself, related to the ion beam species, implantation energy, substrate composition, surface quality, etc.) and the probability of the SEDs producing a sufficient signal for positive detection (related to the SED gain configuration, which is explored experimentally in Supporting Information, Section S.1).

Determination of detection efficiency, η, for the current work is based on the method previously described [21]. For a series of ion beam pulses, the average number of detections per pulse, v, can be used to determine η:

$$v = -\ln\left(\frac{M-p}{M}\right) = \eta\lambda \tag{3}$$

TABLE 1 | Detection data for 50 keV P into intrinsic silicon through a native oxide layer, with an ion beam current of 148 ± 7 fA. The values for $s(v_i t_i)$ and $s(t_i^2)$ are determined using the linear regression method outlined in [17]. The switching latency was calculated to be 4 ns, which is used to find the adjusted pulse width ($t = T - T_o$) for the calculation of λ.

Set Pulsewidth, T, μs	λ, ions pulse^{-1}	Num. Attempts,	v_i	$s(v_i t_i)$	$s(t_i^2)$
0.21	0.0951	33 773	0.0769	6823	18 631
0.42	0.1921	18 013	0.1494	7014	19 717
0.63	0.2891	11 587	0.2430	6449	16 716
0.84	0.3861	9324	0.3121	6673	17 958
1.05	0.4831	7517	0.4043	6404	16 631
1.26	0.5801	6506	0.4849	6370	16 551
1.47	0.6771	5938	0.5465	6560	17 646
1.68	0.7741	5215	0.6527	6211	15 985
1.89	0.8711	4723	0.7536	5982	15 002
2.10	0.9681	4462	0.8216	6042	15 443

where p is the number of successful detections from M attempted implantations.

In the work presented here, the ion beam current was fixed and λ is varied by changing the pulse width. The number of required positive detections for experiment completion, p, was maintained at 2500 (determined by implantation into a 50 × 50 point array as described in the Experimental Methods section) allowing statistically significant data to be obtained. The number of pulses required to record the 2500 positive detections varied, depending on three main factors: (i) the average number of ions in a given pulse, λ; (ii) the emitted secondary electron yield for the ion implanted into a substrate (which varies based on the ion beam and substrate combination); and (iii) the efficiency of the detection mechanism.

2.1 | Linear Regression

The software analysis of the SED signal, described above, is binomial (for each ion pulse delivered an implantation event is either detected or not detected) and as v scales its error also scales, therefore linear regression is appropriate in the determination of the error in the average number of detections per pulse, v [17].

An example of detection efficiency data for 50 keV P (25 kV anode voltage, Wien filter selecting the doubly charged ion, P^{2+}) into silicon (through a native oxide layer) is shown in Table 1. The pulse width was varied for a fixed ion beam current (148 ± 7 fA) and the number of pulse attempts to create an array of 2500 successful detections was recorded. The representative number of ions per μs, N, with its associated error, δN were obtained using:

$$N = \frac{S(vt)}{S(t^2)} \tag{4a}$$

$$\delta N = \frac{1}{\sqrt{S(t^2)}} \tag{4b}$$

$S(vt)$ and $S(t^2)$ are obtained using:

$$S(vt) = \sum_i s(v_i t_i) = \sum_i \frac{v_i t_i}{s(v_i)^2} \tag{5a}$$

$$S(t^2) = \sum_i s(t_i^2) = \sum_i \frac{t_i^2}{s(v_i)^2} \tag{5b}$$

where $s(v_i t_i)$ and $s(t_i^2)$ are the uncertainties in the product of v and t, and t with itself, respectively, for each iteration (i) of λ, where the pulse length, T is corrected by the switching latency; 4 ns for the ion energy used in Table 1. Using the number of attempted pulses for a given iteration of λ (M_i) and average number of detections per pulse (v_i) the uncertainty $s(v_i)$ is obtained:

$$s(v_i) = \sqrt{(e^{v_i} - 1)/M_i} \tag{6}$$

The detection efficiency, η, can then be determined using the expression:

$$\eta = \frac{N}{L} \tag{7}$$

where L is the number of ions per μs, determined using Equation (2), with $t = 1$ μs. For the data presented in Table 1, the detection efficiency is calculated to be 82 (±4)%, the uncertainty for which comes from the error propagation of L and N.

The detection efficiency calculated here is representative of the probability of successfully detecting an ion implantation event for a specific point. This can be extended to obtain the probability of successfully creating a doped array of single ions. As the array size increases, the probability of failure in creating a perfect array of single-ion-implanted points also increases [17]. However, it is feasible that devices may be constructed from imperfect arrays, where a number of sites have multiple ions or missing implantations and the use of such an imperfect array being countered by future quantum error correction codes [23]. It is therefore useful to ensure as high a success rate as possible whilst also having some knowledge of regions where single, multiple, and no ions have been implanted. This will also provide a route to future direct verification of the measured detection efficiency via STEM of implanted membranes, for example.

2.2 | Direct Peak Counting

As λ approaches 1 ion per pulse, the probability of having a single pulse containing more than one ion follows Poissonian statistics,

increasing significantly. The possibility of implanting multiple ions when one is required is undesirable for the utilisation of the implanted ions as qubits, as unwanted ion–ion interaction can lead to qubit decoherence. This can be countered by reducing λ, for example, from 1 to 0.1, which reduces the probability of an ion pulse containing more than 1 ion from ~26% to ~0.47%. However, there are practical limitations to how small a λ may be obtained, particularly regarding the ion source stability when operating in low beam current modes.

Even with the use of low values for λ, the ability to distinguish a single ion implantation from a multiple ion implantation event is desirable, which becomes possible with the utilisation of high-bandwidth SED electronics. Figure 2a provides examples of the detector output recorded for two ion pulses where successful detection occurred using the high-bandwidth detectors. One trace (Figure 2a(i)) shows a single sharp peak corresponding to a single ion implantation, while the other (Figure 2a(ii)) shows two distinct sharp peaks, corresponding to two ions being implanted during the single pulse. The insets in Figure 2a show the signals within the detection window; the time within which a signal must be detected in order to register as a positive detection. The additional low intensity peaks observed at 0.085 and 1 µs following the sharp initial peak consistently appear and arise as artefacts due to the high bandwidth detection electronics.

Through counting the number of peaks recorded within each detection window (j), it is possible to map the number of implanted ions across the array for each value of λ. Figure 2b shows such a map obtained for 50 keV P doping into silicon using $\lambda = 0.1$ ions per pulse. Table 2 shows that as λ increases, the proportion of the 2500 successful detections that have a higher number of ion events increases, in line with what is expected from Poissonian statistics.

There is a discrepancy between the experimentally determined percentage of pulses containing a particular number of peaks (j) and that predicted by Poissonian statistics. This arises due to the detection inefficiencies and the stochastic nature of secondary electron emission. It is possible to adjust the predicted (Poissonian) values with a scalar (S) such that a closer agreement with the experimentally observed values is obtained. Equation (8a) shows the scaled Poisson probability as a function of number of ions, $p(j)$, per pulse that is non-zero. Equation (8b) takes into account the proportion of predicted pulses that are missed by the detector and therefore, registered as empty pulses.

$$p(j) = S\left(\frac{\lambda^j \exp(-\lambda)}{j!}\right), \qquad j > 0 \tag{8a}$$

$$p(0) = \exp(-\lambda)(1-S)\sum_{j=1}^{6}\left(\frac{\lambda^j \exp(-\lambda)}{j!}\right) \tag{8b}$$

The scalar for which the difference between the experimental values and the scaled Poissonian values is smallest (maximum difference of 2.34%, Tables S.1 and S.2 in Supporting Information, Section S.2) is 0.93, indicating a 93% confidence in detection and peak prediction. This method of determining the number of ions implanted into a substrate assumes that each ion arrives at the substrate independently of any other ions within a given pulse, and does so within the set pulse width (typically greater than 200 ns, as per Table 1).

3 | Detection Efficiency

The detection efficiencies were determined for a variety of ions, implanted into a number of different substrates, using the linear regression method outlined above. For each ion species, two ion acceleration voltages of 12.5 and 25 kV were used, with the latter being the maximum anode voltage of the P-NAME tool used for this work [6]. Selection of the ion species' charge state using the Wien filter enabled access to ion implantation energies of 12.5 keV (singly-charged ion, 12.5 kV anode), 25 keV (either doubly-charged ion and 12.5 kV anode, or singly-charged ion and 25 kV anode), and 50 keV (doubly-charged ion, 25 kV anode). Ion cluster implantation (e.g., Au_2^+) was also investigated for a limited number of cases to further explore the relationship between ion beam configuration and detection efficiency.

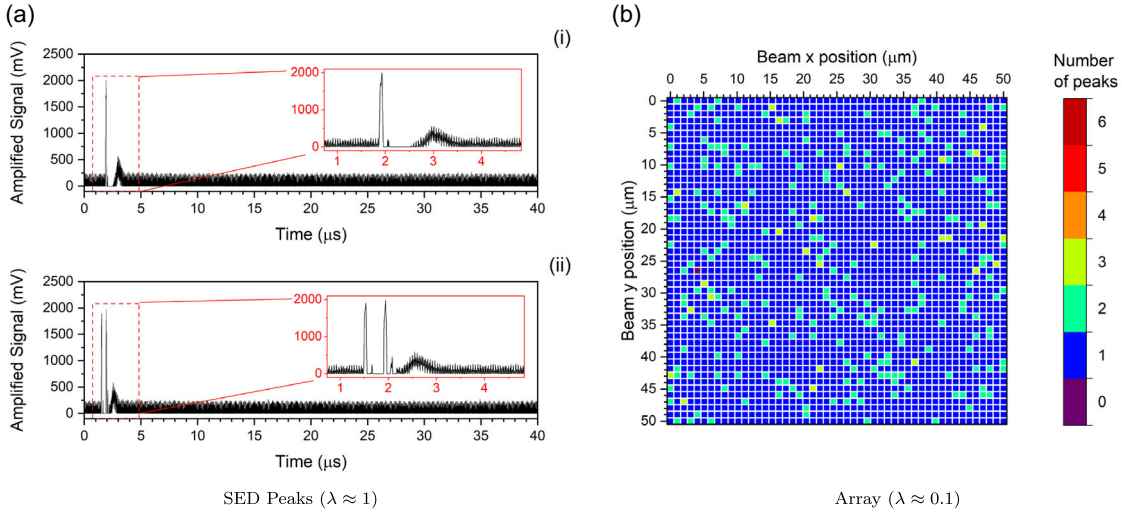

FIGURE 2 | (a) Example SED traces showing (i) single and (ii) double ion implantation events as a result of ion pulses with $\lambda = 1$. The inset highlights the detection window, set as the time within which a signal must be detected in order to register as a successful implantation event. (b) Map of the number of ion implantation events detected at each point within a 50×50 point array during deterministic doping of 50 keV P into silicon for $\lambda = 0.1$.

TABLE 2 | Percentage of total pulses for each value of λ which contain a particular number (j) of peaks for the 50 keV P implantation into silicon dataset. Numbers in the brackets are the percentage probabilities of a pulse containing that particular number of ions, given by Poissonian statistics.

	% of pulses with j peaks, experimental (Poissonian)						
λ (ions pulse^{-1})	0	1	2	3	4	5	6
0.0951	93 (91)	6 (9)	1 (0)	0 (0)	0 (0)	0 (0)	0 (0)
0.1921	86 (83)	12 (16)	2 (2)	0 (0)	0 (0)	0 (0)	0 (0)
0.2891	78 (75)	18 (22)	3 (3)	1 (0)	0 (0)	0 (0)	0 (0)
0.3861	71 (68)	23 (26)	5 (5)	1 (1)	0 (0)	0 (0)	0 (0)
0.4831	65 (62)	26 (30)	7 (7)	1 (1)	0 (0)	0 (0)	0 (0)
0.5801	60 (56)	29 (32)	9 (9)	2 (2)	1 (0)	0 (0)	0 (0)
0.6771	55 (51)	31 (34)	11 (12)	3 (3)	1 (0)	0 (0)	0 (0)
0.7741	51 (46)	32 (36)	12 (14)	3 (4)	1 (1)	0 (0)	0 (0)
0.8711	44 (42)	35 (36)	14 (16)	5 (5)	1 (1)	0 (0)	0 (0)
0.9681	42 (38)	33 (37)	16 (18)	6 (6)	2 (1)	0 (0)	0 (0)

3.1 | Silicon

Figure 3 shows the detection efficiencies for the various ion species when implanted into silicon (through a native oxide layer). Increasing the implantation energy from 12.5 to 50 keV (Figure 3a) results in an increase in the detection efficiency across all the ion species investigated.

In Figure 3b, a common implantation energy of 25 keV is achieved using two different anode voltages by selecting the charge of the ions. Whilst there is a variation in the absolute value of detection efficiency between the singly- and doubly-charged ion states, in the cases for which a comparison may be made (Si, P, Co, Ge, Au, and Bi), the figures fall within each others error bounds. This indicates that for this range of ion species, and at this energy, the charge state of the ion does not strongly impact the secondary electron emission from silicon and therefore ion detection efficiency. For the lower energies studied (12.5 and 25 keV), there is a decrease in detection efficiency as ion mass increases until Ge, after which no further significant reduction occurs. Interestingly, this trend is not observed at the higher energy used (50 keV).

3.2 | Silicon Dioxide

Figure 4 shows the detection efficiencies for the various ion species implanted into SiO_2. The detection efficiency values fall within the range of 70%–100% for all the ion beam species explored. As the implantation energy is increased, there is an increase in detection efficiency (Figure 4a). The effect of ion charge state variation, for the same implantation energy (Figure 4b), reveals no distinct variation in detection efficiency for the two charge states beyond the error bounds of the measurements. Unlike for silicon, no consistent relationship between ion mass and detection efficiency is observed at any energy used.

Comparing the measured detection efficiencies between silicon and SiO_2 (200 nm SiO_2 on boron-doped silicon, see Experimental Methods for more details) reveals that all of the efficiencies in the oxide sample are greater than those measured in silicon with only a native oxide. Since the oxide thickness is too great for any of the ions of the energies investigated in this work to pass through the oxide layer and stop in the underlying silicon layer of the SiO_2, the increase in detection efficiency is expected to result from the oxide nature of the substrate. This is discussed in further detail below.

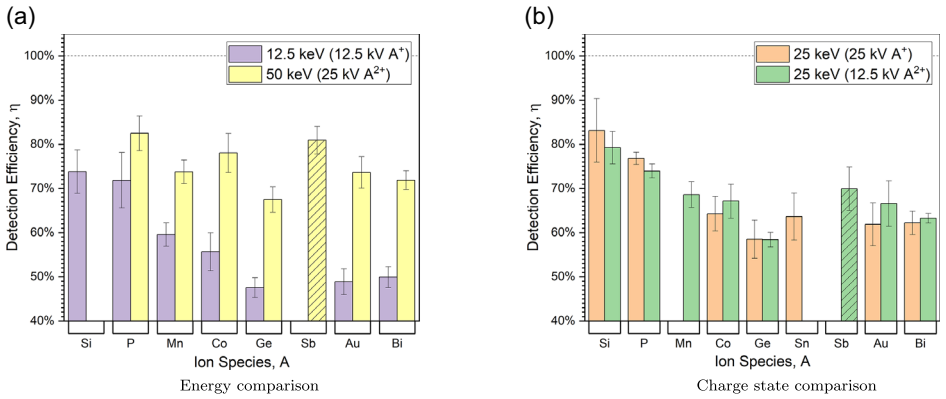

FIGURE 3 | Detection efficiency measurements for various ion species into undoped silicon (through a native oxide layer). (a) The anode voltage and charge state of the ions was varied to obtain different implantation energies, and (b) the same implantation energy. Hashed bars represent data that was previously reported [24].

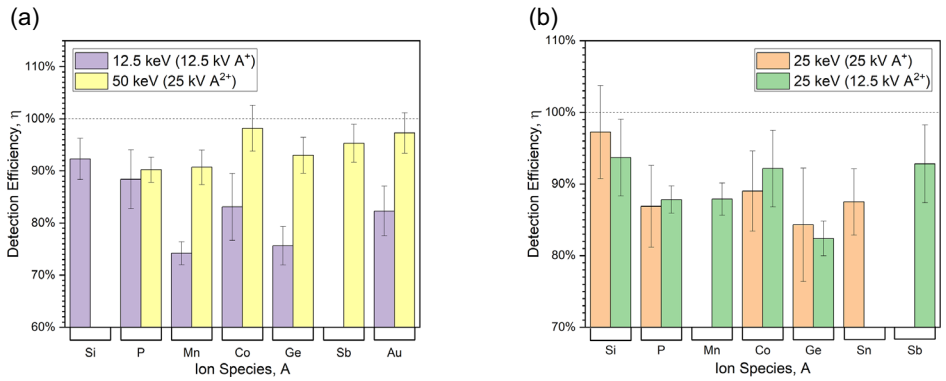

Energy comparison

Charge state comparison

FIGURE 4 | Detection efficiency measurements for various ion species into SiO_2. (a) The anode voltage and charge state of the ions was varied to obtain different implantation energies, and (b) the same implantation energy.

3.3 | Aluminium Oxide

In the case of Al_2O_3, Figure 5a reveals that for a number of ions, there is not a significant increase in detection efficiency as the energy is increased, the only exception being Ge. Some values of the detection efficiency (e.g., 50 keV Sb and 25 keV Si, singly-charged variation) are above 100%, due to minor ion beam current variation during the experiment. The errors in these results account for this uncertainty, with the lower bounds showing that the detection efficiency values in all cases are at or below 100%.

The effect of changing ion charge state (Figure 5b) shows greater variation in the detection efficiencies, with the majority of singly-charged ions (Si, P, Mn, and Ge) all having higher detection efficiencies than their doubly-charged counterparts. Conversely, Co stands out as the only species with a higher detection efficiency when a doubly-charged ion is implanted, though this is possibly due to contamination on the substrate in the region for the 25 kV Co^+ experiment (discussed further below). Au in Al_2O_3, as with the silicon substrate, has very similar absolute detection efficiency values, for the doubly-charged ion, the error bounds are more significant.

The detection efficiencies measured for implantation into Al_2O_3 are comparable to, if not greater than, those measured for SiO_2. This indicates that the oxide nature of these two substrates results in a higher secondary electron yield and therefore greater detection efficiency for the ions investigated here, relative to the non-oxide substrates. Similarly, no strong dependence of the detection efficiency on ion mass is observed.

3.4 | Gallium Arsenide

There is a significant increase in the detection efficiency for ion implantation into GaAs as the implantation energy increases (Figure 6a), with Au showing the greatest increase. The trend of reduction in detection efficiency with increasing ion mass at an energy of 12.5 keV is also present here. This decreasing trend is also observed at an energy of 25 keV, and similar to that observed for silicon, ceases for masses greater than Ge.

Considering the error bounds in Figure 6b, the variation of ion charge state does not have a significant impact on the detection efficiency, with the possible exception of P, which has a lower efficiency for the doubly-charged case.

3.5 | Diamond

Figure 7a shows that P implantation into diamond does not demonstrate a significant increase in detection efficiency as the energy is increased, while the rest of the ions investigated do. However, P shows a statistically significant decrease in

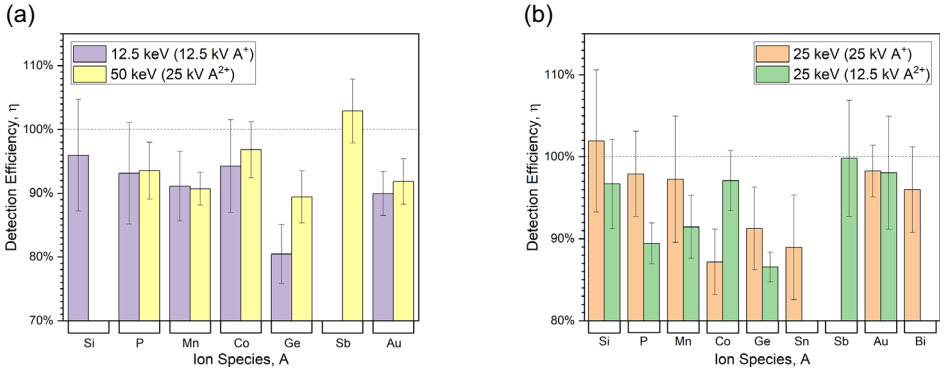

Energy comparison

Charge state comparison

FIGURE 5 | Detection efficiency measurements for various ion species implanted into Al_2O_3. (a) The anode voltage and charge state of the ions was varied to obtain different implantation energies, and (b) the same implantation energy.

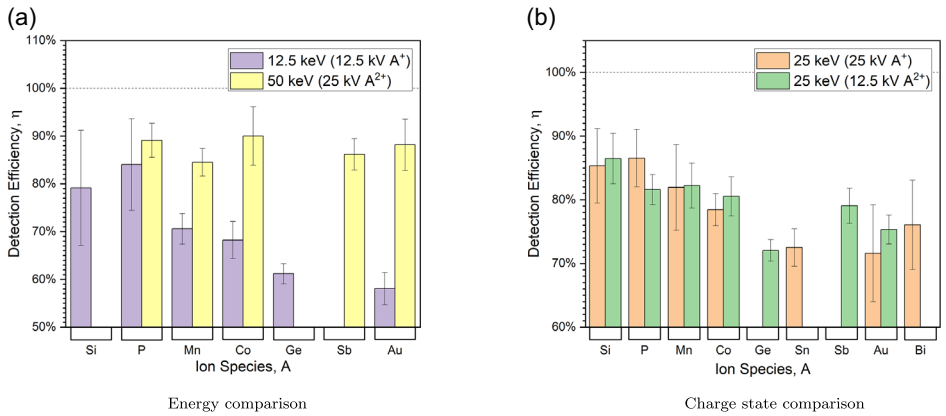

FIGURE 6 | Detection efficiency measurements for various ion species implanted into GaAs. (a) The anode voltage and charge state of the ions was varied to obtain different implantation energies, and (b) the same implantation energy.

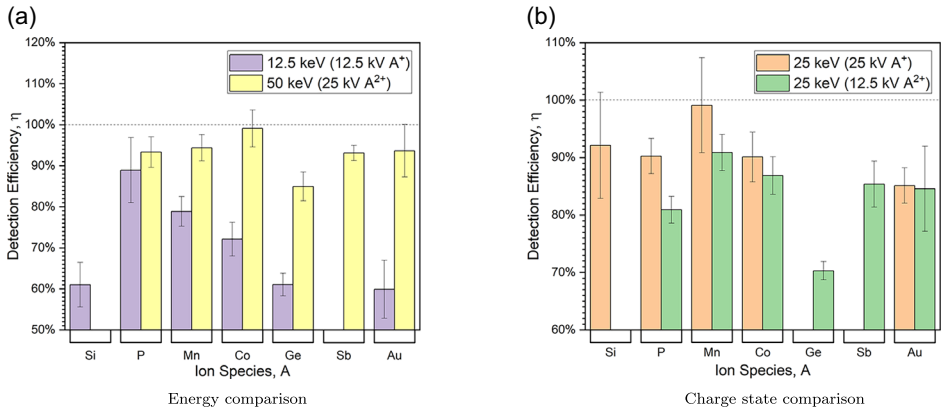

FIGURE 7 | Detection efficiency measurements for various ion species implanted into diamond. (a) The anode voltage and charge state of the ions was varied to obtain different implantation energies, and (b) the same implantation energy.

detection efficiency when the charge state is increased for the same implantation energy (Figure 7b). Mn, Co, and Au also show a decrease in efficiency as the charge state is increased, though within their respective error bounds. As discussed for GaAs, at 12.5 keV, there is a similar dependence (except for Si) of the detection efficiency on ion mass up until Ge is reached. The implantation of Si results in a similar increase in detection efficiency when the energy is doubled from 12.5 to 25 keV, as is observed when increasing the Au implantation energy from 12.5 to 50 keV.

3.6 | Silicon Carbide

The detection efficiencies of SiC also decrease with increasing ion mass when comparing fixed implantation energies and extending to Bi, the heaviest ion used, (Figure 8a). Increasing the implantation energy is consistently found to improve the detection efficiency for all ions implanted into SiC, with the greatest difference being observed between the 12.5 and 50 keV Au implantation, dominated by the low detection efficiency at 12.5 keV. Figure 8b shows that, with the exception of Mn, there is no significant difference in the detection efficiencies of singly- and doubly-charged ions. It is also observed that the implantation of Sn into SiC gives the lowest detection efficiency (35%) observed in this study.

3.7 | Cluster Implantations

The detection efficiency for ion cluster implantation was investigated (non-exhaustively) as part of this work. For all of the ion clusters studied, an anode voltage of 25 kV was chosen, with the exception of Bi_2^+, which was also investigated for 12.5 kV implantation into silicon (demarcated with an asterisk in Figure 9).

There are two Sb clusters presented in Figure 9, one of which is a typical cluster formed from two of the same isotope (specifically ^{123}Sb, which was the Sb isotope used in the single-ion detection efficiency measurements in this work) with a single shared charge. The other, however, is a unique doubly-charged cluster formed from a single ion of each Sb isotope ($^{121}Sb^{123}Sb$), which has been investigated in more detail elsewhere [24]. This doubly-charged Sb cluster has a mass-charge ratio (the key parameter in isotopic selection via mass-filtering) of 122 amu e^{-1}, which means it lies between the two main singly-charged Sb peaks (121 amu e^{-1} and 123 amu e^{-1}, previously reported in [6]). The presence of this doubly-charged mixed-isotope cluster indicates that similarly doubly-charged cluster isobars of $^{121}Sb_2^{2+}$ and $^{123}Sb_2^{2+}$ ions are present in the mass-selected singly-charged beam, since the mass-charge ratios are equal. Therefore, by selecting $^{121}Sb^+$, one would also be implanting with $^{121}Sb_2^{2+}$. Since it is not possible to select a singly-charged Sb ion without also selecting the cluster, which is

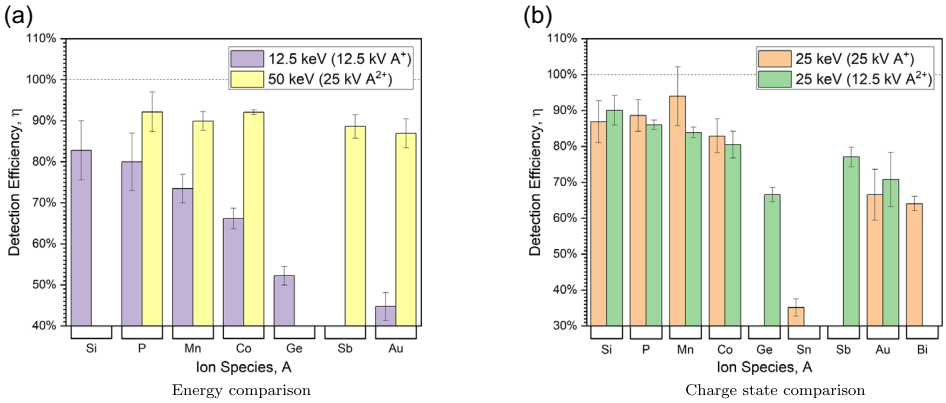

FIGURE 8 | Detection efficiency measurements for various ion species implanted into silicon carbide. (a) The anode voltage and charge state of the ions was varied to obtain different implantation energies, and (b) the same implantation energy.

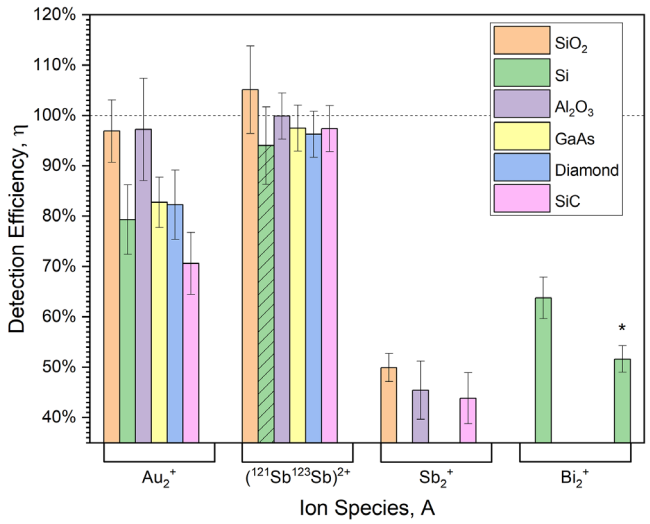

FIGURE 9 | Detection efficiency measurements for various ion species into different substrates defined in the legend. Hashed bars represent data that was previously reported [24]. All ion clusters were implanted with an anode of 25 kV, with the exception of the second Bi_2^+ (demarcated with an asterisk, *), which was implanted with an anode voltage of 12.5 kV.

not ideal in applications of single ion (or even single cluster) implantation, no singly-charged Sb implantations have been investigated in this work. The hashed bar in Figure 9, and in the silicon data presented above in Figure 3, represents detection efficiency data we have previously reported [24].

Comparison of the ion cluster detection efficiency data presented in Figure 9 with the single-ion data presented above is possible by considering the energy per atom for the species being implanted. For example, a 25 keV Au_2^+ is presumed to implant with 12.5 keV per atom within the cluster, which can be compared with the 12.5 keV Au^+ ion implantation presented above. When using this comparison, the 25 kV clusters Au_2^+, $(^{121}Sb^{123}Sb)^{2+}$, and Bi_2^+ (non-asterisk data in Figure 9) can be compared with 12.5 kV ions Au^+, Sb^{2+}, and Bi^+, respectively.

Doing so, it is observed that most of the detection efficiencies for the ion-clusters are greater than for their single-ion counterpart. The greatest variation was found in the case of 25 kV Au_2^+ compared to 12.5 kV Au^+ (both 12.5 keV per atom) into silicon, where the cluster was found to lead to a 30% increase in detection efficiency (79 (±7)% and 49 (±3)%, respectively).

The smallest (non-zero) difference is found for 25 kV Au_2^+ implantation into Al_2O_3, where a 7% increase in detection efficiency was found when comparing to the 12.5 kV Au^+, with efficiencies of 97 (±10)% and 90 (±3)%, respectively. No difference was found between 25 kV $(^{121}Sb^{123}Sb)^{2+}$ compared to 12.5 kV Sb^{2+} in Al_2O_3, where both resulted in a value of 100 (±5)%.

4 | Si Oxide Thickness Variation

The results above show that in all cases there is a gain in detection efficiency for ion implantation into SiO_2 relative to silicon (with a native oxide layer) for the same ion beam species (mass, charge, and energy). However, the thickness of the oxide layer in these results is too thick (200 nm) to allow the low-energy ions studied in this work (≤50 keV) to stop in the underlying silicon substrate, where they would need to end up in order to be useful in buried dopant qubit applications.

Thinner oxide growth is standard practice in CMOS device fabrication, and likewise is a necessary stage in the fabrication of buried dopant qubit devices (gate oxides, in particular). It is, therefore, of interest to determine the detection efficiency gain of thinner SiO_2 layers.

Dry thermal oxide growth was used to grow SiO_2 layers of various thicknesses on undoped silicon (see Experimental Methods for more details), and ellipsometry was used to verify the thicknesses (see Supporting Information, Section S.3). Due to their direct application in qubit technologies, only P and Sb implantation were explored for these samples. The energy per ion used was chosen for study was 50 keV (the maximum available) and 8 keV as the minimum. The latter was chosen for implanting P ions closer to the surface (≈16 nm) and within the range required for addressing spins using electric fields (using single electron transistors, for example [25]). The same minimum energy per ion was used for the Sb cluster for the sake of comparison.

Figure 10 shows a general increase in detection efficiency across all energies of P and Sb as the thickness increases from native (3.23 (±0.17) nm) to the thinnest grown oxide (44.97 (±0.18) nm). The range of thicknesses grown here still results in the P and Sb ions stopping in the oxide layer, with the exception

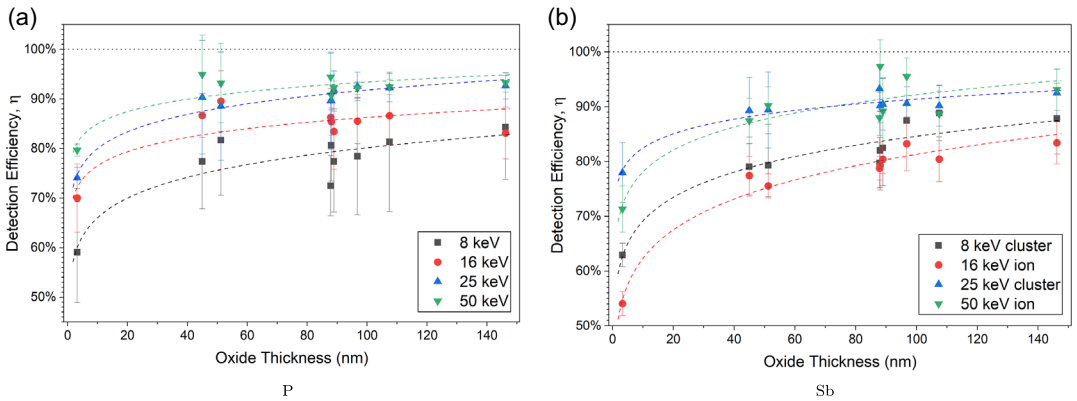

FIGURE 10 | Detection efficiency measurements for various thickness of oxide grown on undoped silicon for the range of energies stated in the legend. (a) Shows the singly- and doubly-charged P ions (8 kV P^{2+} for 16 keV, etc.), while (b) shows doubly charged in all cases (8 keV achieved with a doubly-charged cluster at 8 kV anode voltage). The dashed lines are to guide the eye, and the horizontal dotted line indicated 100% detection efficiency.

of 50 keV P, which stops a few nm past the silicon-SiO_2 interface, though with an even thinner oxide than grown here, it is possible for the ion to stop further in to the silicon substrate.

The fabrication of qubit devices in silicon will greatly benefit from ^{28}Si enrichment [7, 8, 26], which results in extended qubit coherence times [27]. The implantation doses required to reach such a high degree of enrichment when using FIB leads to significant amorphisation, requiring annealing in order to recover the crystalline environment in which the dopant may operate as a qubit. However, it is advantageous to implant the donor ion into the amorphous enriched material, which can increase the electrical activation of the donor during annealing to deliver epitaxial crystal regrowth [28]. We therefore investigated the ion detection efficiency as a function of ^{28}Si enrichment (and thereby amorphisation) for 16 keV P implantation. We observed no significant gain or reduction in detection efficiency from using natural (unenriched, crystalline) through to highly enriched (1E19 ions cm^{-2}, amorphous) silicon (see Supporting Information, Section S.4 for more information).

5 | Discussion

In the data reported above, we have demonstrated the ability to form an implanted array of 2500 ions with high detection efficiency for a number of ion-substrate combinations. Specifically, arrays of 50 keV ^{31}P doped directly into silicon are achieved with 82 (±4)% efficiency of detection for a positive implantation signal, with 89% of these positive detection signals resulting in a single SED peak (correlating with a single ion implantation). A detection efficiency of 81 (±3)% is found when implanting 50 keV ^{123}Sb into silicon. Both of these ions are of immediate technological interest when implanted into silicon for utilisation as donor qubits. Implanting these same ions into SiO_2 on silicon yields a detection efficiency of 90 (±2)% and 95 (±4)% for 50 keV ^{31}P and ^{123}Sb, respectively. This relationship between increased detection efficiency and thickness of SiO_2 is explored further with ^{31}P and ^{123}Sb into various thicknesses of SiO_2 thermally grown on silicon. These results show that only a few tens of nm of SiO_2 on silicon are required in order to achieve the secondary electron emission gain. Recent work using atomic layer deposition (ALD) to form SiO_2 layers on silicon has found an increased single ion implantation detection efficiency with only a few nm of SiO_2 [29]. Engineering a thin oxide for increased detection efficiency would enable a device fabrication process flow that would facilitate the creation of large arrays of buried dopant qubits within minutes using this doping method.

Of the other substrates investigated here which are of immediate technological interest, the highest detection efficiencies are found in diamond. Of the group IV elements which are useful for creating colour centres in diamond, only Si and Ge have results presented in this work, with 25 keV Si (achieved with singly-charged 25 kV Si) showing the greatest detection efficiency (~92%), though with a large error. With such a high detection efficiency, it is of interest to investigate the deterministic implantation of large-scale arrays coupled with methods of deterministic colour centre activation, particularly laser annealing [9], which can lead to a higher yield than that expected from thermal annealing techniques (e.g., 8.6% for SnV [30]). This would have the added benefit of being site-selective, allowing for feedback throughout the annealing process. Combining deterministic ion implantation and direct laser annealing will enable a full exploration of the defect complexes that form, aiming toward the goal of colour centre formation on demand with nanoscale spatial precision.

SiC, like diamond, can form colour centres attributed to defects and vacancies which may be introduced through ion implantation [31]. Similar to diamond, the ability to implant single ions with high detection efficiencies can provide the opportunity to investigate single and ensemble defects in SiC, and the emission characteristics thereof for engineering emitters in quantum applications at room temperature [32].

Similar to silicon, GaAs and Al_2O_3 have also been investigated as hosts for ion spin systems for applications in quantum computation [33] and memory [34], respectively. While the detection efficiencies for GaAs on the whole are not necessarily as high as other substrates, the spin systems of interest (Mn, for example) still have a high enough detection efficiency to warrant the use of secondary electron detection for single ion implantation. Al_2O_3, like SiO_2, has amongst the highest detection efficiencies reported in this work, alluding to a particular property of oxides which leads to a greater secondary electron emission than in non-oxide materials.

The most important factor influencing the detection efficiency is the secondary electron yield, which is related to the implanted ion species and substrate combination. Since the SEDs are

comprised of channeltron electron multipliers (to amplify the secondary electrons to an appreciable and detectable signal), information about the secondary electron emission, such as the number of collected secondary electrons, their energy, and direction of emission, etc., is not available. However, comparisons between the detection efficiencies obtained here and previous trends in secondary electron emission may still be made.

The trend of increasing secondary electron yield as the implantation energy [35] and cluster size [36] are increased is well established for a range of ion species and substrate combinations. Previous studies into secondary electron emission with various gaseous ion species and charge states have seen an increase in secondary electron emission as the charge state is increased [37]. In contrast, the charge state variation investigated in this study, using non-gaseous species, does not result in a significant increase in detection efficiency.

When considering the effect of using different substrates, no significant correlation between measured detection efficiency was found with respect to conductivity, band gap, ionisation energy, or density. The electronic and nuclear stopping powers of ions implanted into substrates were simulated using the Monte Carlo simulation package, SRIM (Stopping Ranges of Ions in Matter [22]). The stopping powers for the ion species and substrates of interest as a function of implantation energy are plotted in Figure S.3 (Supporting Information, Section S.5), we found no significant correlation between the stopping powers (or ratios and differences thereof) and the detection efficiencies measured in this work.

Surface roughness has also been observed to have an effect on secondary electron yield variation [38, 39]. This may account for some observed results which show variation from the otherwise observed trend, particularly with respect to samples for which a significant difference in detection efficiency was found when using different charge states but with the same implantation energy which is not observed for other species or substrates. Another explanation for outliers in this respect is surface contamination, which would result in a varied secondary electron yield compared to a cleaner region of the substrate. While great care was taken to ensure the substrates were thoroughly cleaned, it is possible that small regions of contamination either persisted or were introduced prior to the sample loading process.

Whilst there is an increase in detection efficiency for cluster implantation relative to the single-ion implantation, for applications in single atom devices, like qubits following the Kane proposal, implanting clusters will guarantee that the ion of interest for encoding of the qubit state will be in close proximity to a second ion, potentially resulting in decoherence. This is assuming that the two ions within the cluster separate by the straggle predicted by the energy per atom in the cluster implantation, which is typically on the order of a few nm in the case of the energies explored in this work [6, 24].

Conversely, when coupled ions are desired, the use of cluster ion implantation with the high efficiency deterministic detection can be advantageous. The cluster implantation and subsequent separation of the atoms on the order of nm may allow for the overlap of electron wavefunctions. This allows for the coupling of the nuclear spins of the adjacent ions via the shared electron, resulting in a three-qubit system. This has been previously demonstrated with pairs of P ions in a silicon-based device, which had been subject to single ion implantation and a pair of P ions in close proximity fortuitously found [40]. While P clusters have not been considered in the work presented here, the P-NAME system is able to access such a cluster and is expected to follow the trend of increased detection efficiency for the cluster compared to the single-ion implantation (72 (±6)% for 12.5 keV P in silicon).

Another ion species of interest for solid-state qubit systems, particularly in silicon, is Sb. The potential for application of mono-atomic and coupled (by cluster implantation) Sb qubits in silicon has been discussed previously [24], with the coupling of the high nuclear spin Sb ions via a shared electron expected to realise a larger Hilbert space onto which quantum information may be encoded than the coupled P or mono-atomic Sb systems [41].

Schneider et al. [29] observe a decrease in detection efficiency as the mass of the incoming ion increases, which we also observe in the results presented here in the vast majority of cases. In their work, Schneider et al. suggest a relationship between detection efficiency and substrate properties, namely the energy required to generate a free electron, electronic stopping power, mean escape probability for the potential barrier at the substrate surface, and the electron mean free path. They discuss that while previous simulation and theory work predict a shorter mean free path in SiO_2 than in silicon (which would result in a *lower* secondary electron emission), their results, in line with what we present here, show the opposite to be true.

It is clear that further work will be required to gain a fuller understanding of the effect that ion beam and substrate configuration has on the detection efficiency of single ion implantation, which will include further experimental investigations to complement theoretical treatments. The utilisation of secondary electron emission detection efficiency measurements, as within this work, will facilitate a wide-ranging combination of correlative data which can be used to support theoretical approaches. A fuller understanding in this regard will help to facilitate the engineering of substrates for high-efficiency-single ion implantation for nanoscale photonic and quantum applications.

6 | Conclusion

The detection efficiencies presented provide insight into the confidence with which a single ion (or cluster) may be deterministically implanted. Ion-substrate combinations of immediate technological interest are studied, including those where donor-ion qubit or colour centre formation is desired. For donor creation in silicon, 50 keV deterministic implantation of single P ions is achieved with a detection efficiency of 82 (±4)%, and of ($^{121}Sb^{123}Sb$) with an efficiency of 94 (±8)%. When these same ions were implanted into SiO_2, the detection efficiency saw a marked increase of 90 (±2)% and 105 (±8)% for the P ion and Sb cluster, respectively. In diamond, the detection efficiency of Ge was found to be 70 (±2)%. These results are comparable to those obtained using IBIC detectors of similar energies, only without the requirement for electrodes specifically for the detection mechanism, confirming that deterministic ion implantation using secondary electron emission is a viable route to flexible and scalable qubit array fabrication.

7 | Experimental Methods

7.1 | Deterministic Ion Implantation

The P-NAME ion implantation system (Q-One, Ionoptika Ltd.) has a maximum anode voltage of 25 kV, with a variety of elements available through the use of a range of liquid metal alloy ion sources (LMAISs). The mass selectivity of the P-NAME system allows for the selection of a specific element from the source alloy with isotopic resolution [6]. The implanted ion species was controlled using the Wien filter to select the ion mass and charge-state for a particular variation of the anode voltage.

Electrostatic plates within the ion beam column were used to provide ion pulsing, enabling the ion beam to be exposed to the substrate in pulses of controlled width. Two high-sensitivity secondary electron detectors within the main sample chamber of the P-NAME system were oppositely biased to attract and detect charged particles: one biased for secondary electrons and negatively charged ions, and the other for positively charged secondary ions (see Supporting Information, Section S.1 for gain optimisation data). The ion beam current in the sample space was measured prior to and following each experiment using a Faraday cup. To mitigate ion source instability impacting the analysis, only data where the pre- and post-experiment ion beam current differed by <10% are included in the work presented here. A total of 212 detection efficiency experiments were conducted as part of this work, of which only 17 had to be omitted due to such variation.

Each experiment was configured to implant an array of ions into 50×50 points, with a 1 μm pitch. The ion beam was directed to each point by adjusting the positioning voltages with the beam blanked. Once positioned, the beam blanking voltage was removed for the desired time (defining the ion pulse width) with an analogue to digital converter (ADC) simultaneously recording the incoming signal from the two detectors. The secondary electrons emitted from the sample surface and collected by the channeltron detector leading to avalanche amplification of the signal. The ADC continued to record the signal long after the ion pulse ($\sim$40 μs in total). The signal for this pulse was analysed and the coordinate registered as either a "pass" or a "fail". The ion beam was then moved to the next position in the array (with the beam remaining blanked) and the implantation process repeated. The detector gain may be varied through control of the channeltron voltage, with detection efficiencies as a function of gain presented in the Supporting Information, Table S.1. The data and analysis presented within this work were all obtained using identical conditions based on the optimal settings in Table S.1.

Once a full array had been exposed to a single ion pulse, the process was then repeated, returning solely to those positions recorded as a "fail". This sequence was then repeated until all of the points in the array had a recorded "pass", with the number of attempts to complete an entire array being characteristic of the average number of ions per pulse, the detection efficiency, and the secondary electron emission, which is dependent on the ion beam and implanted material in a particular experiment.

The dark count rate was measured by connecting the actively biased SED signal outputs to a single photon counter (Stanford Research Systems, SR400 Two Channel Gated Photon Counter) whilst the ion beam was blanked and recording the number of counts over a period of 2000 s. During this time, 15 171 counts were detected, giving a dark count rate of $\sim$8 dark counts s^{-1}.

7.2 | Samples and Preparation

The undoped silicon (University Wafer) was 500 μm thick (with a native oxide layer), with a resistivity of >10,1000 Ω ·cm, and orientation of <100>. The silicon dioxide on silicon sample (Alpha Nanotech) was boron-doped (as grown, 1–50 Ω ·cm), <100> orientation, with a 200 nm thick SiO_2 top layer. The aluminium oxide (University Wafer) was 430 μm thick, C to M plane orientation. The GaAs (MCP Wafer Technology Ltd.) was 500 μm thick, undoped, and <100> orientation. The diamond (Element Six) was CVD-grown electronic grade. The SiC (MSE Supplies) sample was 500 μm thick, semi-insulating 4H.

Prior to loading into the P-NAME system, all samples were subject to a cleaning process of ultrasonication, twice in acetone for 2 min then once for 2 minutes in IPA, followed by blow-drying with nitrogen gas. The clean samples were fixed to aluminium sample plates using copper adhesive tape away from the implantation sites (with the exception of the diamond sample, which was adhered using a double-sided adhesive carbon tab due to the size of the sample). These sample plates were then loaded onto the P-NAME sample platen for the duration of the experiments while the relevant LMAIS sources were in operation, and stored in sample storage boxes otherwise.

The SiO_2 samples for the oxide thickness variation were thermally grown in a Carbolite TF dry oxidation furnace under a constant nitrogen flow of 0.5 litres per minute. The furnace was heated at a rate of 10°C per minute, to a temperature of 1100°C, at which point oxygen was introduced at a flow rate of 0.12 litres per minute. Different oxide thicknesses were grown by varying the duration for which the substrates were exposed to this temperature and gas flow and the thicknesses were verified with ellipsometry (see Supporting Information, S.3).

Acknowledgements

This work was supported by funding from the UK EPSRC grant EP/V001914/1.

Funding

This study was supported by Engineering and Physical Sciences Research Council (EP/V001914/1).

Conflicts of Interest

The authors declare no conflicts of interest.

Data Availability Statement

The data that support the findings of this study are available from the corresponding author upon reasonable request.

References

1. J. Kim, D. Min, J. Cho, et al., "A Fault-Tolerant Million Qubit-Scale Distributed Quantum Computer," in *Proceedings of the 29th ACM International Conference on Architectural Support for Programming Languages and Operating Systems* (2024), 1–19.

2. Y. He, S. Gorman, D. Keith, L. Kranz, J. Keizer, and M. Simmons, "A Two-Qubit Gate between Phosphorus Donor Electrons in Silicon," *Nature* 571, no. 7765 (2019): 371–375.

3. J. Wyrick, X. Wang, R. V. Kashid, et al., "Atom-by-Atom Fabrication of Single and Few Dopant Quantum Devices," *Advanced Functional Materials* 29, no. 52 (2019): 1903475.

4. X. Yu, B. Wilhelm, D. Holmes, et al., "Schrödinger Cat States of a Nuclear Spin Qudit in Silicon," *Nature Physics* 21, no. 3 (2025): 362–367.

5. A. M. Jakob, S. G. Robson, H. R. Firgau, et al., "Scalable Atomic Arrays for Spin-Based Quantum Computers in Silicon," *Advanced Materials* 36, no. 40 (2024): 2405006.

6. M. Adshead, M. Coke, G. Aresta, et al., "A High-Resolution Versatile Focused Ion Implantation Platform for Nanoscale Engineering," *Advanced Engineering Materials* 25, no. 22 (2023): 2300889.

7. R. Acharya, M. Coke, M. Adshead, et al., "Highly 28si Enriched Silicon by Localised Focused Ion Beam Implantation," *Communications Materials* 5, no. 1 (2024): 57.

8. M. Coke, M. Adshead, R. Acharya, et al., "Fabrication of Planar Highly Enriched Silicon by ^{28} Si Focused Ion Beam and Subsequent Experimental Optimization," *Advanced Electronic Materials* 11 (2025): e00233.

9. X. Cheng, A. Thurn, G. Chen, et al., "Laser Activation of Single Group-Iv Colour Centres in Diamond," *Nature Communications* 16, no. 1 (2025): 5124.

10. G. Tosi, F. A. Mohiyaddin, V. Schmitt, et al., "Silicon Quantum Processor with Robust Long-Distance Qubit Couplings," *Nature Communications* 8, no. 1 (2017): 450.

11. R. Hull, J. Floro, J. Graham, et al., "Synthesis and Functionalization of Epitaxial Quantum Dot Nanostructures for Nanoelectronic Architectures," *Materials Science in Semiconductor Processing* 11, no. 5-6 (2008): 160–168.

12. M. Choi, S. Jun, K. Y. Woo, et al., "Nanoscale Focus Pinspot for High-Purity Quantum Emitters via Focused-Ion-Beam-Induced Luminescence Quenching," *ACS Nano* 15, no. 7 (2021): 11317–11325.

13. D. Blight, M. Adshead, A. Prencipe, M. Sanaee, K. Gallo, and R. J. Curry, "Ion-Implanted Erbium in X-Cut Thin-Film Lithium Niobate: Luminescence and Low-Temperature Response," arXiv preprint arXiv:2511.04442 (2025).

14. M. Hollenbach, N. Klingner, N. S. Jagtap, et al., "Wafer-Scale Nanofabrication of Telecom Single-Photon Emitters in Silicon," *Nature Communications* 13, no. 1 (2022): 7683.

15. J. M. Smith, S. A. Meynell, A. C. Bleszynski Jayich, and J. Meijer, "Colour Centre Generation in Diamond for Quantum Technologies," *Nanophotonics* 8, no. 11 (2019): 1889–1906.

16. S. Pezzagna, B. Naydenov, F. Jelezko, J. Wrachtrup, and J. Meijer, "Creation Efficiency of Nitrogen-Vacancy Centres in Diamond," *New Journal of Physics* 12, no. 6 (2010): 065017.

17. B. Murdin, N. Cassidy, D. Cox, R. Webb, and R. J. Curry, "Error Rates in Deterministic Ion Implantation for Qubit Arrays," *physica status solidi (b)* 258, no. 6 (2021): 2000615.

18. N. F. L. Collins, A. M. Jakob, S. G. Robson, et al., "Graphene-Enhanced Single Ion Detectors for Deterministic Near-Surface Dopant Implantation in Diamond," *Advanced Functional Materials* 33, no. 51 (2023): 2306601.

19. J. L. Pacheco, M. Singh, D. L. Perry, et al., "Ion Implantation for Deterministic Single Atom Devices," *Review of Scientific Instruments* 88, no. 12 (2017): 123301.

20. A. M. Jakob, S. G. Robson, V. Schmitt, et al., "Deterministic Shallow Dopant Implantation in Silicon with Detection Confidence Upper-Bound to 99.85% by Ion-Solid Interactions," *Advanced Materials* 34, no. 3 (2022): 2103235.

21. N. Cassidy, P. Blenkinsopp, I. Brown, et al., "Single Ion Implantation of Bismuth," *Physica Status Solidi (a)* 218, no. 1 (2021): 2000237.

22. J. F. Ziegler, M. D. Ziegler, and J. P. Biersack, "Srim-the Stopping and Range of Ions in Matter, 2010," *Nuclear Instruments and Methods in Physics Research Section B: Beam Interactions with Materials and Atoms* 268, no. 11-12 (2010): 1818–1823.

23. P. Steinacker, N. Dumoulin Stuyck, W. H. Lim, et al., "Industry-Compatible Silicon Spin-Qubit Unit Cells Exceeding 99% Fidelity," *Nature* 646 (2025): 81–87.

24. M. Adshead, M. Coke, E. Tillotson, et al., "Isotopically Selected Co-Doping of ^{121}Sb and ^{123}Sb Pairs in Silicon," *Advanced Materials* (2026): e22240.

25. D. Holmes, B. Wilhelm, A. M. Jakob, et al., "Improved Placement Precision of Donor Spin Qubits in Silicon Using Molecule Ion Implantation," *Advanced Quantum Technologies* 7, no. 3 (2024): 2300316.

26. D. Holmes, B. C. Johnson, C. Chua, et al., "Isotopic Enrichment of Silicon by High fluence 28 si- Ion Implantation," *Physical Review Materials* 5, no. 1 (2021): 014601.

27. K. M. Itoh and H. Watanabe, "Isotope Engineering of Silicon and Diamond for Quantum Computing and Sensing Applications," *MRS Communications* 4, no. 4 (2014): 143–157.

28. B. L. Crowder, "The Influence of the Amorphous Phase on Ion Distributions and Annealing Behavior of Group Iii and Group v Ions Implanted into Silicon," *Journal of the Electrochemical Society* 118, no. 6 (1971): 943.

29. E. B. Schneider, O. G. Lloyd-Willard, K. Stockbridge, et al., "Enhanced Secondary-Electron Detection of Single-Ion Implants in Silicon through Thin SiO_2 Layers," *Nano Letters* 26 (2026): 795–800.

30. T. Lühmann, R. John, R. Wunderlich, J. Meijer, and S. Pezzagna, "Coulomb-Driven Single Defect Engineering for Scalable Qubits and Spin Sensors in Diamond," *Nature Communications* 10, no. 1 (2019): 4956.

31. T. Kobayashi, M. Rühl, J. Lehmeyer, L. K. Zimmermann, M. Krieger, and H. B. Weber, "Intrinsic Color Centers in 4hr-Silicon Carbide Formed by Heavy Ion Implantation and Annealing," *Journal of Physics D: Applied Physics* 55, no. 10 (2021): 105303.

32. M. Widmann, S.-Y. Lee, T. Rendler, et al., "Coherent Control of Single Spins in Silicon Carbide at Room Temperature," *Nature Materials* 14, no. 2 (2015): 164–168.

33. J.-M. Tang, J. Levy, and M. E. Flatté, "All-Electrical Control of Single Ion Spins in a Semiconductor," *Physical Review Letters* 97, no. 10 (2006): 106803.

34. I. Wisby, S. De Graaf, R. Gwilliam, et al., "Angle-Dependent Microresonator Esr Characterization of Locally Doped Gd^{3+}: Al_2O_3," *Physical Review Applied* 6, no. 2 (2016): 024021.

35. Y. Chutopa, B. Yotsombat, and I. G. Brown, "Measurement of Secondary Electron Emission Yields," *IEEE Transactions on Plasma Science* 31, no. 5 (2003): 1095–1099.

36. K. Baudin, A. Brunelle, S. Della-Negra, J. Depauw, Y. Le Beyec, and E. S. Parilis, "Sublinear Effect in Electron Emission from Solids Bombarded with Swift Gold Clusters," *Nuclear Instruments and Methods in Physics Research Section B: Beam Interactions with Materials and Atoms* 117, no. 1-2 (1996): 47–54.

37. H. Eder, M. Vana, F. Aumayr, and H. Winter, "Precise Total Electron Yield Measurements for Impact of Singly or Multiply Charged Ions on Clean Solid Surfaces," *Review of Scientific Instruments* 68, no. 1 (1997): 165–169.

38. V. Baglin, J. Bojko, C. Scheuerlein, et al., "The Secondary Electron Yield of Technical Materials and Its Variation with Surface Treatments," Tech. Rep. (2000).

39. H. Seiler, "Secondary Electron Emission in the Scanning Electron Microscope," *Journal of Applied Physics* 54, no. 11 (1983): R1–R18.

40. M. T. Mądzik, S. Asaad, A. Youssry, et al., "Precision Tomography of a Three-Qubit Donor Quantum Processor in Silicon," *Nature* 601, no. 7893 (2022): 348–353.

41. I. Fernández de Fuentes, T. Botzem, M. A. I. Johnson, et al., "Navigating the 16-Dimensional Hilbert Space of a High-Spin Donor Qudit with Electric and Magnetic Fields," *Nature Communications* 15, no. 1 (2024): 1380.

Supporting Information

Additional supporting information can be found online in the Supporting Information section.